Soft Matter

Cite this: *Soft Matter*, 2012, **8**, 1776

www.rsc.org/softmatter

PAPER

Direct correlation between creep compliance and deformation in entangled and sparsely crosslinked microtubule networks†

Yali Yang,‡[a] Jun Lin,‡[b] Bugra Kaytanli,[a] Omar A. Saleh[bc] and Megan T. Valentine*[a]

Received 15th September 2011, Accepted 28th November 2011
DOI: 10.1039/c2sm06745e

The microtubule cytoskeleton is essential in maintaining the shape, strength and organization of cells and its misregulation has been implicated in neurological disorders and cancers. To better understand the structure-mechanics relationships in microtubule networks, we measure the time- and force-dependent viscoelastic responses of entangled and sparsely crosslinked microtubule networks to precise microscale manipulation. We use magnetic tweezers devices to apply calibrated step stresses and measure the resultant strain as a function of time. At short times the material behaves as an elastic solid. The linear regime is large, with gentle stiffening observed in entangled networks above ~70% strains. Crosslinked networks are stiffer, and show an extended linear regime. At longer times, we find a creeping regime, suggesting that structural rearrangements of the network dominate the mechanical response. To understand the molecular origins of this behaviour, we use a newly-developed portable magnetic tweezers device to observe the network morphology using a confocal microscope while simultaneously applying point-like stresses to embedded magnetic particles. We observe substantial network compression in front of the bead with no evidence of long-length scale filament flow, and find that the spatial extent of the deformation field depends sensitively on network architecture and connectivity. Our results are important to understanding the role of the cytoskeleton in regulating cargo transport *in vivo*, as well as the basic physics of non-affine deformations in rigid rod polymer networks.

Introduction

The microtubule (MT) cytoskeleton is a complex biopolymer network found ubiquitously in eukaryotes. MTs play important roles in cell division, where they move chromosomes and localize the cleavage furrow, and in intracellular transport where they form the tracks upon which the transport of secretory/synaptic vesicles, organelles, and other cargo occurs.[1] There is increasing evidence that the spatiotemporal organization of the MT cytoskeleton is essential for numerous other biological processes, ranging from axonal branching and neural pathfinding,[2,3] to the flow of actin in motile and developing cells,[4,5] to the regulation of protein synthesis.[6] For many of these processes, mechanical stress within the MT cytoskeleton is an important signalling mechanism: for example, tension promotes MT outgrowth at focal adhesion sites,[7] regulates MT turnover and organization,[8] and silences spindle assembly checkpoints to enable cell cycle control.[9]

In contrast to many biological polymers, mechanical measurements of isolated MTs have shown them to be extremely stiff. MTs are long hollow cylinders with an average contour length of order ~10 μm, large outer diameter of ~25 nm, and persistence length of ~1000 μm.[10,11] Because of this, MT networks lack the entropic contributions of elasticity that dominate the mechanical response of most polymer gels, and are ideal model systems for athermal, rigid rod polymer materials. A limited number of prior studies have investigated the rheological properties of entangled or crosslinked networks of MTs.[12–15] The most comprehensive study investigated networks of fairly short MTs (characteristic length <3 μm) under uniform shear conditions. These were found to be soft elastic solids that softened above strains of ~10% and showed evidence of transient attractive filament–filament interactions that enhanced elasticity and suppressed reptation-induced terminal relaxation.[13]

In the current work, we explore the microscale mechanical response of networks of longer MTs (average length ~23 μm) subjected to highly localized forces applied using a magnetic tweezers device. This generates a non-uniform deformation field, with a characteristic bending radius dictated by the size of the embedded magnetic particles (~5 μm).[16] In this regime, filament

[a]*Department of Mechanical Engineering, University of California, Santa Barbara, CA, USA. E-mail: valentine@engineering.ucsb.edu; Fax: +805-893-8651; Tel: +805-893-2594*
[b]*Biomolecular Science and Engineering Program, University of California, Santa Barbara, CA, USA*
[c]*Department of Materials, University of California, Santa Barbara, CA, USA*

† Electronic supplementary information (ESI) available. See DOI: 10.1039/c2sm06745e

‡ Authors contributed equally to this work.

bending dominates over stretching or compression, thus the physical origins of elasticity, dissipation, and nonlinearity differ from that of networks in which all deformations are affine. Thus, mean-field models that require uniform stretching or bending of filaments no longer apply, limiting the use of traditional continuum mechanics approaches for modeling.[17] This motivates the development and use of new characterization tools that enable direct measurement of structure–property relationships.

Here, we show that upon sudden application of force, entangled MT networks are predominantly solids, with modest time-dependent network reorganization occurring at longer times. To understand the molecular origins of this behaviour, we observe the three-dimensional MT network morphology using a confocal microscope, while simultaneously applying localized stresses to embedded magnetic particles. We find that the network is substantially compressed in front of the bead, and observe no obvious long-length scale flow of material, suggesting that subtle reorganization of entanglements dominates the creep response. These results have important implications for understanding the mechanical properties of the cytoskeleton, in which rigid networks of MTs and actin bundles are locally deformed by transport of intracellular cargos, as well as large-scale structural changes in cell division, motility and morphogenesis. Importantly, we find that the spatial extent of the deformation field can be modulated by inclusion of a small number of rigid cross-linkers. This suggests that even sparse connections between filaments can play an essential role in regulating cell mechanics.

Results

Microstructural properties of entangled and crosslinked microtubule networks

One challenge in determining structure-mechanics relationships in soft biopolymer materials is the difficulty in generating homogeneous materials that can be imaged and mechanically manipulated without damage. To address this, we have developed a robust polymerization method that allows small volumes of MT networks to be generated in a chamber amenable to both fluorescence confocal imaging and manipulation by magnetic tweezers. We load ice-cold solutions of globular tubulin dimers into small capillary tubes in the presence of GTP (required for the enzymatic addition of tubulin) and Taxol (a small molecule that promotes MT assembly), then seal and incubate the tubes at ~35 °C for ~1 h to induce polymerization. For mechanical measurements, magnetic and latex beads are added to the solutions prior to loading and samples are rotated to prevent bead settling during the polymerization reaction. This protocol reliably produces MTs with mean filament length of ~23 μm. Although the MT length distribution is fairly broad, it is nearly independent of tubulin density, with good agreement observed even for the tails of the distribution that represent the longest filaments (Fig S1, ESI†). This reproducibility is critical, since even a small number of long filaments can have a disproportionately strong effect, particularly in the non-affine deformation regime.[18] By developing a protocol that results in a robust and concentration-independent length distribution, we can easily isolate effects due to MT density from effects due to changes in polymer length. Moreover, the long average length ensures that filaments are able to form multiple connections with neighbouring filaments, and thus generate fully entangled gels.

Representative images of entangled MT networks, with concentrations ranging from 5 μM to 20 μM are shown in Fig. 1. For each condition, images are thresholded to generate a binary map of 'bright' pixels on a dark background. The spatial distribution of distances between nearest neighbour bright pixels is determined. The decay length of this exponential distribution gives the characteristic network mesh size, ξ.[19,20] We find ξ to decrease monotonically with increasing tubulin concentration, with $\xi \sim c^{-3/4}$ (Fig. 1). This scaling relationship is surprising, as it is generally expected that mesh size will scale with the inverse square root of concentration, due to geometric arguments for filament crossing.[21] Although we do not understand the physical origins of this difference, our results are very reproducible, and we have not found any other experimental demonstration of mesh size scaling for MT networks that contradict this result. Upon crosslinking (using streptavidin and biotinylated tubulin), networks appear more heterogeneous, with the formation of tubulin-dense and tubulin-poor regions throughout the sample, and the characteristic mesh size increases slightly.

Local mechanical perturbations are used to probe microscale viscoelastic properties of MT networks

To determine the microscale viscoelastic properties of entangled MT gels, we polymerize the networks in the presence of small magnetic particles, then apply controlled loads varying from 0–35 pN using a magnetic tweezers device (representative data trace is shown in Fig. S2, ESI†).[22] The magnetic field is supplied by a pair of permanent magnets whose position is varied to control the magnetic force at the sample plane. We choose to examine three tubulin concentrations: 18 μM, 26 μM, and 51 μM. We use magnetic particles with diameter of 4.5 μm, which is larger than the mesh size in each case to ensure that the particles are fully engaged with the meshwork and their displacement can be interpreted in terms of local network mechanical response. It is difficult to measure the mechanical properties of gels formed with lower tubulin concentrations because 4.5 μm beads tend to slip through the mesh, and the fragile networks do not easily support the weight of larger beads. Gels are observed *via* fluorescence confocal microscopy prior to each mechanical measurement to ensure that network quality is maintained from day to day. We measure particle displacement as a function of applied force, as previously described.[22,23]

A typical creep response is shown schematically in Fig. 2. When the force F is stepped up by the rapid motion of the magnets toward the sample, the bead position instantaneously jumps a distance d_1, indicating a short-time elastic response. The bead displacement then slowly increases, indicating a long-time creep regime with average velocity v. The crossover time from the elastic regime to the creep regime is given by the time constant τ. After a time T, which is typically 50–75 s, the force is abruptly stepped down to zero by rapid retraction of the magnets, and the bead position rapidly jumps back a distance d_2 to a final position given by Δx_f. After waiting a time that is typically comparable to T, another force pulse is applied. In order to maintain network quality, we complete all mechanical measurements within a few hours of forming the gels, and thus use the minimum waiting

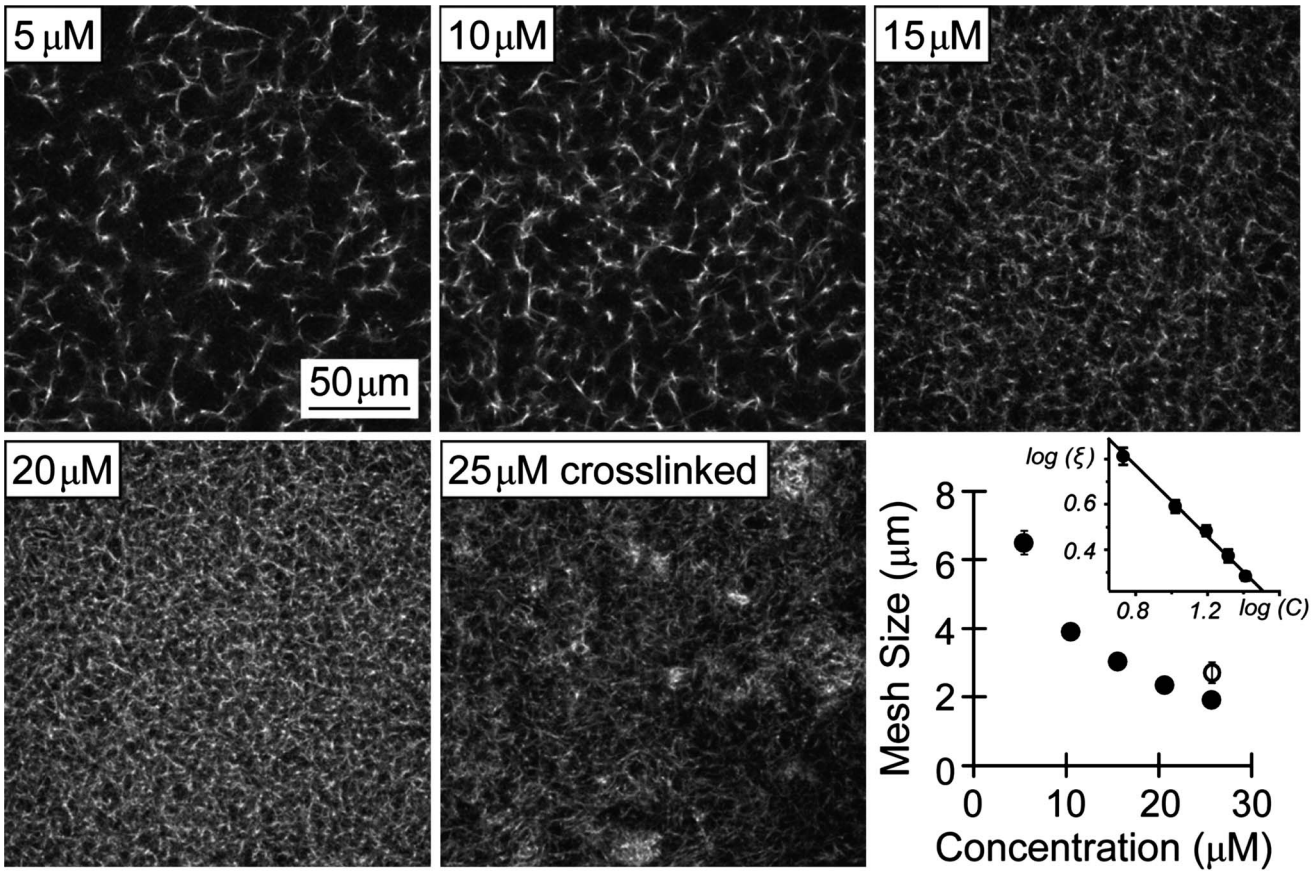

Fig. 1 Representative images of entangled and crosslinked MT networks obtained using fluorescence confocal microscopy. Under our polymerization conditions, the entangled MT networks are isotropic and homogeneous. Mesh size is found to decrease monotonically with increasing tubulin concentration (solid symbols). Upon addition of crosslinkers, networks appear to be more structurally heterogeneous, and the average mesh size increases slightly (open symbol). Inset: Data plotted on a log-log plot, and fit to a power law $\xi \sim c^{-\alpha}$ (fit shown in solid line) where α is found to be 0.76 ± 0.02.

time that gives us reproducible results in order to maximize the throughput of our data collection. We have doubled both T and the waiting time between pulses and found no obvious effect on measured mechanical parameters.

To understand the molecular origins of network viscoelasticity and gain insight into the structure-mechanics relationships of these gels, we use a newly-developed portable magnetic tweezers device,[24] which allows imaging of fluorescently-labelled MT networks using confocal microscopy while simultaneously applying controlled loads. As shown in the upper panel of Fig. 2 and discussed in detail below, we find substantial compression of the MT network in front of the bead, and a rarefied network behind. We do not observe flow of polymeric material nor do we find any evidence of shear alignment of filaments near the particle, even under fairly high forces (>20 pN). We tested for effects of loading history by repeatedly applying the same force or by ramping the force up and then back down as a function of time, and in both cases we find a negligible effect on measured mechanical properties.

Additionally, we do not find evidence of nonspecific binding of microtubules to the magnetic beads: the network density at the bead surface is not enhanced before the force is applied, as we would expect if the bead was acting as a local nucleator or crosslinking site, and no filaments appear to remain attached at the rear of the bead when force is applied. We do occasionally observe abrupt motions of beads as they escape from the local cage of MTs that form the meshwork at the sphere surface, particularly at low polymer density or high force. When identified, these abrupt slip events are excluded from analysis in order to isolate predominantly mechanical interactions from those dominated by local microstructure.

Entangled MT networks are mechanically elastic on short time scales

Network stiffness can be estimated by dividing the applied force F by instantaneous bead displacement d_1, as shown in Fig. 3. We choose to present the localized elastic response in terms of gel stiffness, to distinguish the microscale mechanical response, which likely depends on the geometry of the network–probe interface, from the scale-invariant continuum elastic modulus. At small forces, the stiffness is nearly constant indicating an approximately linear elastic response (Fig. 3A). For forces greater than ~15 pN, gentle stress stiffening is observed for each tubulin concentration. This gentle transition is clearer when stiffness is plotted as a function of strain, which we approximate

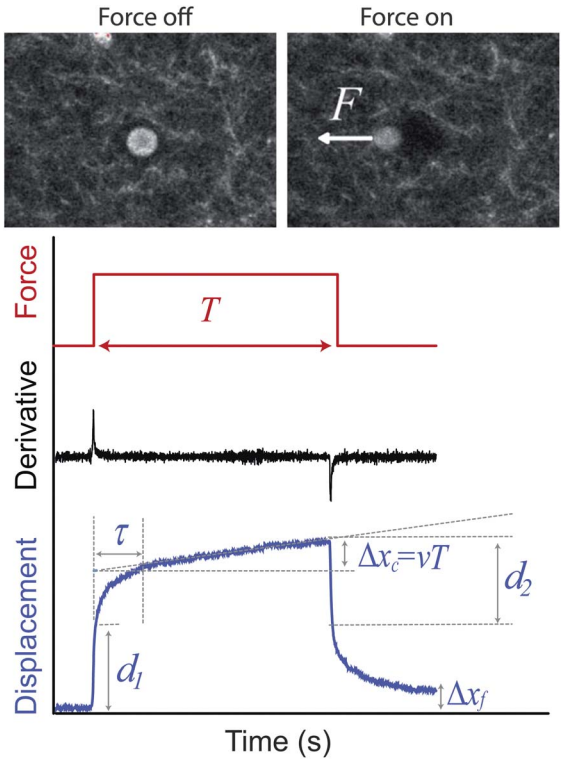

Fig. 2 Schematic of typical creep response curve. The upper panel shows two representative images of a 4.5 μm diameter magnetic bead embedded in an entangled MT network at zero force (left) and F ≈ 10 pN obtained with our newly-developed portable magnetic tweezers device. The lower panel shows a typical creep response curve. Bead displacement x (blue line) and the force pulse F (red line) are plotted as a function of time t. At short times, the bead responds elastically, followed by a relaxation into a creeping regime. To identify the onset of relaxation, we calculate the derivative of $x(t)$-vt (black line), which exhibits a maximum at the transition from elastic to creep regime. The typical range of applied forces is 1–30 pN, which induces micron-scale bead displacements.

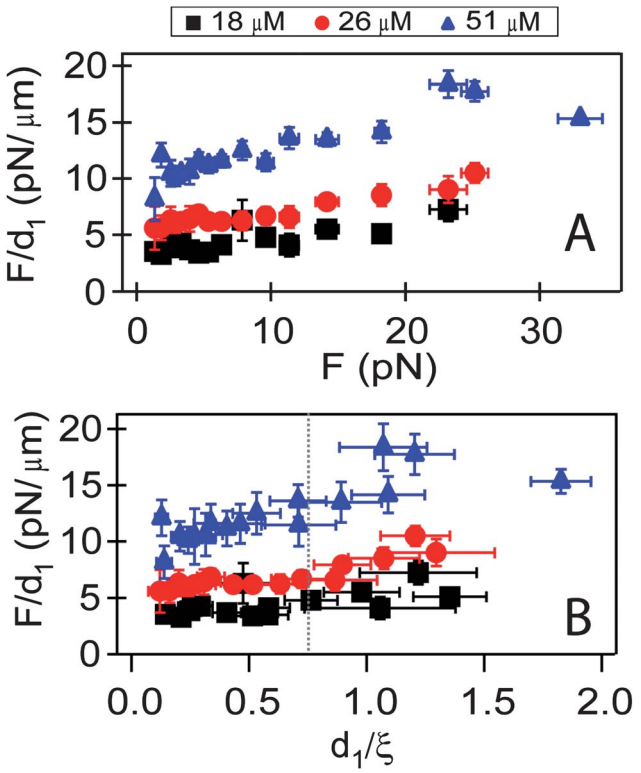

Fig. 3 Entangled MT stiffness, given by F/d_1 as a function of (A) force and (B) strain, d_1/ξ. At low forces or strains network stiffness is roughly constant, while mild stiffening is observed for F above ~15 pN or strains greater than ~70% (dotted line).

by dividing the jump distance d_1 by the network mesh size ξ that we determined *via* confocal microscopy. In this case, we see stiffening above strains of ~70% (as indicated by the dotted line in Fig. 3B). We find that the maximal force we can reliably apply to the network increases monotonically with tubulin concentration. At larger forces, beads tend to escape from the local cage of MTs that form the meshwork at the sphere surface, preventing measurement of gel properties.

At low forces (and strains) the network shows a force- (and strain-) independent plateau. In this regime, stiffness increases linearly with tubulin concentration, as shown in Fig. 4. This behaviour is consistent with networks of rigid rods, in which each new filament contributes equally to network elasticity, and contrasts that of entropic networks such as those formed from semiflexible entangled actin filaments, where stiffness tends to arise due to the stress-induced straightening of thermally-undulating filaments.[25] This suggests that entangled MT networks are primarily mechanical (enthalpic) networks. Similar trends are observed for the elastic transition in which force is abruptly stepped down to zero, as shown in Fig. S3 (ESI†).

Interestingly, we find that for large forces F > 15 pN, the bead jump distances upon application and removal of the force (d_1 and d_2, respectively) are not equal; rather $d_2 > d_1$, with the strongest decrease observed for the most dense MT network (Fig. 5). This suggests that at large forces, the network is permanently deformed upon application of force, and that the network the

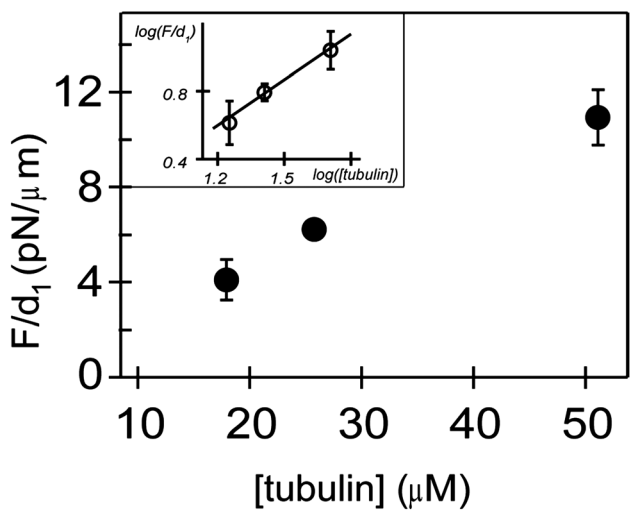

Fig. 4 MT stiffness depends linearly on tubulin concentration. This indicates that the elastic response is dominated by mechanical, rather than entropic, stretching of polymer filaments. Inset: Data plotted on a log–log plot, and fit to a power law $F/d_1 \sim [\text{tubulin}]^{\alpha}$ (fit shown in solid line). α is found to be 1.0 ± 0.3.

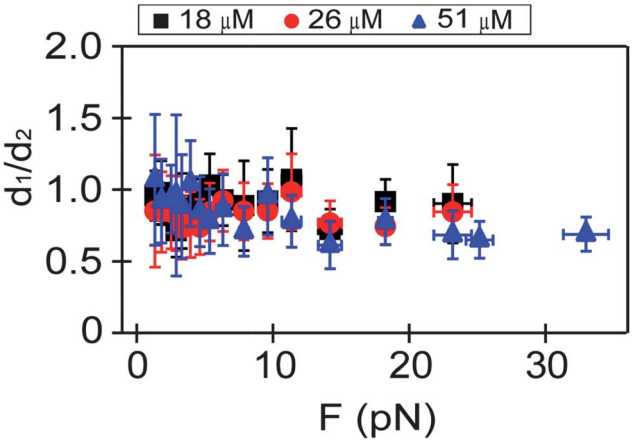

Fig. 5 Particle position before and after force step. (A) The ratio of d_1/d_2 is plotted as a function of force for each entangled MT network. At the lowest forces, this ratio is approximately equal to 1, consistent with a linear elastic regime. For force above the critical force for stress stiffening (~15 pN), we find $d_2 > d_1$ with the strongest decrease observed for the densest MT network.

bead returns to when force is stepped down to zero is mechanically and structurally different than the original network that enclosed the bead. It is likely that $d_2 > d_1$ because the application of force leads to an asymmetry in polymer concentration at the bead surface. When the force is turned on, the bead engages with and compresses the network in front, whereas when the force is turned off, the bead returns to the original position through a large void.

On long time scales, entangled MT networks are restructured

After the initial elastic regime, there is a crossover, on a time scale τ of ~10 s for all conditions studied, to a regime in which bead position increases linearly with time. This creep regime indicates a modest time-dependent rearrangement of the sample that might arise due to filament reorganization, bond breakage, or mechanical slippage of the bead through the network. Creep velocity v increases linearly as a function of force for each tubulin concentration (Fig. 6). Using Stokes' Law $F = \gamma v$, we can determine an effective drag coefficient γ as a function of tubulin concentration. We find γ to nearly double when the tubulin concentration is increased from 18 μM to 26 μM, but no significant change in γ when the concentration is further increased to 51 μM.

To further investigate the origins of this creep regime, we compare the total distance the bead moves during the creeping phase $\Delta x_c = vT$ to the unrecovered displacement Δx_f (see Fig S4†). As expected from our analysis of the creep velocity, Δx_c increases monotonically with applied force. For small forces, $\Delta x_f \approx \Delta x_c$, and both are on the order of ~100 nm, much smaller than the bead diameter or ξ, but larger than our estimated tracking error. We suspect this distance is determined by the time-averaged thermal fluctuations of the bead. At larger forces, $\Delta x_f \gg \Delta x_c$ due to force-induced slippage of the bead through the porous network. This allows some beads to become trapped in new "pores" when the force is turned off, with higher forces required to induce bead entrapment in denser networks.

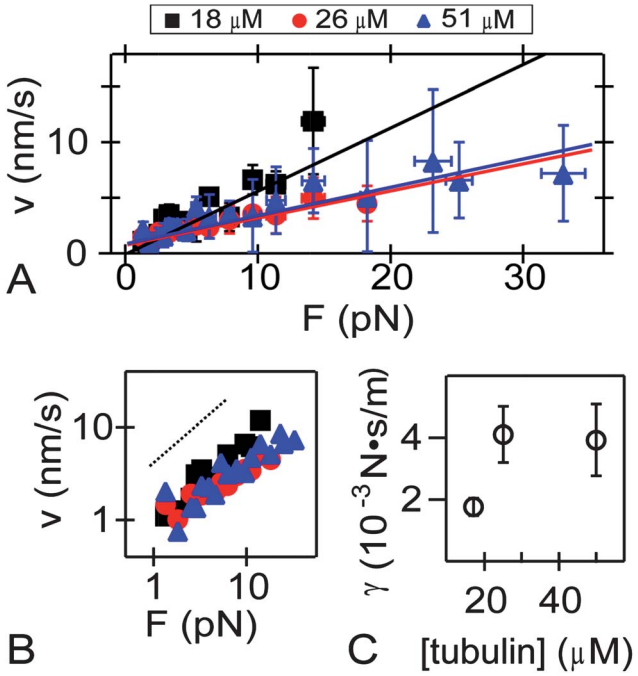

Fig. 6 Analysis of creep regime. (A) Creep velocity is plotted as a function of force for three different tubulin concentrations. (B) In each case, velocity increases linearly with force, as demonstrated by plotting the force-velocity data on a log–log plot. Dotted black line shows slope = 1. (C) Through a linear fit of the force–velocity data (panel A, solid line), an effective drag coefficient can be calculated at each tubulin concentration.

Sparse crosslinking enhances elasticity, suppresses strain stiffening, and increases deformation field penetration depth

To examine the effect of crosslinking on MT networks, we generated sparsely crosslinked gels using biotinylated tubulin and streptavidin. For this work, the total tubulin concentration is fixed at 25 μM, 1 in 7 tubulin dimers is biotinylated, and the ratio of biotin moieties to streptavidin is fixed at 10 to 1. This leads to an average distance between crosslinkers of ~200 nm. We find the gels are roughly twice as stiff as entangled networks at the same tubulin concentration (Fig. 7A), and find no evidence of stress-stiffening for forces up to ~33 pN.

At this modest crosslinker density, we still observe a creep regime, and find the transition time τ and average flow velocity v to be very similar to the values obtained for the 25 μM entangled gels (Fig. 7B). Consistent with our measurements of entangled networks, we find $d_1 < d_2$, although the ratio of d_1/d_2 is roughly constant as a function of force with a mean value of 0.7 ± 0.1.

At these modest crosslinking densities, the strongest mechanical difference between crosslinked and entangled networks is observed when measuring the extent of penetration of the deformation field into the MT network. The spatial extent of deformation is measured in two ways: using small non-magnetic latex beads as fiducial markers that can be visualized using transmitted light microscopy or by directly imaging the MT network using a fluorescence confocal microscope. In both cases, we employ a portable magnetic tweezers device to enable the precision application of force while collecting high-resolution images. As shown in Fig. 8 and Fig. S5 (ESI†), the depth of

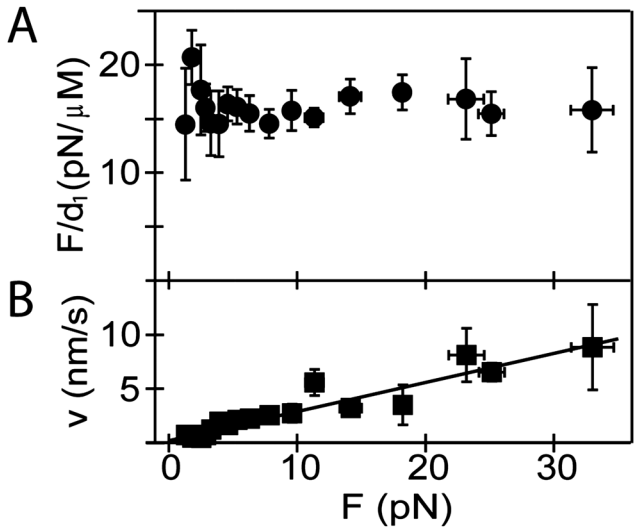

Fig. 7 Mechanical response of sparsely crosslinked 25 μM MT networks. (A) MT stiffness is plotted as a function of force. At low force, the stiffness values are roughly twice those measured for a purely entangled network at the same tubulin concentration. In contrast to entangled networks, the linear regime is large, with no evidence of stress-induced stiffening (or softening) for forces as high as ~33 pN. (B) Creep velocity increases as a function of force, and is very similar in magnitude to that measured using purely entangled networks. The effective drag coefficient is $(3.7 \pm 0.4) \times 10^{-3}$ N s m^{-1}.

penetration is substantially increased upon crosslinking. The typical penetration distance for an entangled network is a few microns, similar to the size of the magnetic particle that is applying the force. By contrast, in crosslinked networks, the deformation field penetrates for tens of microns. This demonstrates that even subtle changes in network architecture and

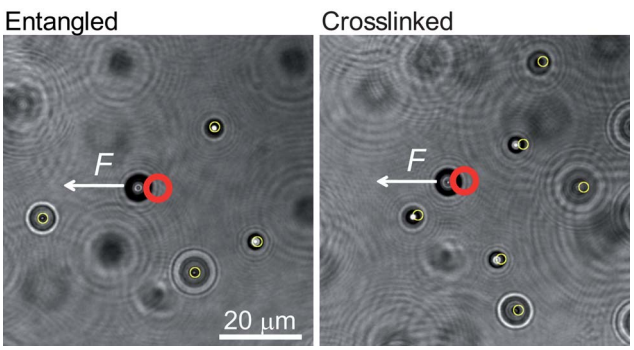

Fig. 8 Network crosslinking substantially increases the ability of deformation fields to penetrate deeply into MT networks. Images show the position of magnetic and latex beads after application of applied force. The original magnetic bead position (with force turned off) is represented by a bold red circle, and original latex bead positions are represented by thin yellow circles for both entangled (left, $F = 25$ pN) and crosslinked (right, $F = 30$ pN) MT gels. The direction of the force is indicated by the white arrow. The entangled gel shows very little deformation away from the magnetic sphere surface, whereas the crosslinked gel demonstrates long-length scale deformation. In the crosslinked case, latex beads separated by >3 magnetic bead particle diameters move substantially, indicating that long wavelength stress transmission is much more efficient in crosslinked networks.

connectivity can have important consequences on stress transmission in MT gels. Moreover, the deformation field is more uniform in the case of the crosslinked gels, indicating that even modest crosslinking can lead to a non-affine to affine network transition.

Discussion

Unlike most biological polymers, we find that MTs form mechanical (enthalpic) networks, whose elasticity arises from bending and stretching of nearly rigid rods. This contrasts the entropic elasticity that dominates the mechanics of individual actin and DNA filaments, and which arises due to the straightening of thermally fluctuating polymers. At low forces, MT networks exhibit a linear elastic response, where network stiffness increases linearly with polymer concentration. At strains >70%, we observe the onset of stiffening for all entangled gels. Although strain stiffening has been observed for many biopolymer networks, it is usually attributed to an entropic-to-enthalpic transition that occurs when the excess length of the flexible or semi-flexible filaments has been fully extended.[26] In the case of MT networks, this stiffening transition must have a different physical origin. Under our loading conditions, we find that a dense accumulation of filaments builds in front of the particle, and a void volume appears behind. We hypothesize that for large localized forces, this accumulation increases the effective polymer concentration near the bead, leading to a nonlinear increase in stiffness. The threshold force associated with the onset of stiffening is ~15 pN, a modest force that could easily be applied by a small number (~3–4) of kinesin motors *in vivo* during cargo transport or mitosis, suggesting this effect may have physiological relevance.

An accumulation of filaments under load was previously reported in magnetic-bead based microrheometry measurements of entangled actin networks.[27] However, in that case there was no evidence of strain stiffening, instead strain softening and force-induced fluidization of the network were observed, suggesting that unlike MT gels, entangled actin networks cannot support large stresses without some form of crosslinking. A number of actin-binding proteins (ABPs) promote the formation of bundles, which can in turn form networks of bundles *in vitro* and in cells. Although these bundles share some similarities with MTs, ABP–actin networks are extremely complex, and it is difficult to compare their rheology to that of entangled MT gels. For example: ABPs are typically dynamic and compliant and thus can contribute substantially to the network response; composite network rheology depends both on actin concentration and the ratio of actin:ABP; ABPs typically crosslink filaments in addition to bundling them giving rise to complex network architecture and topology; bundle formation can occur through aggregation-controlled growth, which can lead to the formation of frustrated out-of-equilibrium structures; and bundle diameter and length is typically polydisperse (and often unknown) leading to numerous length and time scales for stress relaxation.[28–32]

Previous measurements of the rheology of a suspension of very short MTs, with a characteristic length approximately equal to the mesh size, also reported strain softening for strains above ~10%.[13] This suggests that the stiffening behaviour we observe

may require either long MTs that can form truly entangled gels or the application of localized stresses that can lead to the microscale reorganization and densification of the network. Polymer length may be particularly important for rigid rod networks, since the distance between entanglements is much less than the persistence length, allowing a single filament to retain its identity in the network along its entire contour. For each entangled network, we find a transition after ~10 s to a creep regime, in which bead position increases slowly, but linearly with time. This transition time is much too long to describe the drainage time for fluid moving through the porous network, and much too short to describe the time for a thermally-driven filament to reptate along its contour.[33] When we image the network directly under load, we do not find any evidence of shear alignment of filaments or bulk flow of polymers on this (or any other) timescale. We therefore suspect that this time-dependent rearrangement arises from the breakage of weak attractive bonds between neighbouring filaments. Our tubulin proteins are purified by multiple cycles of assembly and disassembly, followed by several rounds of phosphocellulose chromatography to remove any non-functional tubulin dimers and microtubule associating proteins (MAPs). Moreover, we find no evidence of MAP contamination using high-resolution gel electrophoresis or Western blotting, and therefore rule out any MAP-based crosslinking. Instead, we suspect that these attractive interactions may arise from salt bridging or divalent crosslinking mediated by the Mg^{2+} ions that are required for coordination of the GTPase activity of tubulin. Attractive interactions have been reported for other rigid rod suspensions, not only of MTs but also of surfactant-stabilized single walled carbon nanotubes, as well as networks of actin or neurofilaments, two semiflexible polymers.[13,34–39] Identifying the molecular origins of these interactions is a clear future direction for this work.

When a modest number of crosslinks are introduced, we find an increase in gel stiffness and suppression of strain-stiffening, but still observe long-time rearrangement of the sample that is indistinguishable from that of an entangled network at the same polymer density. That suggests that the distance between rigid crosslinks is larger than the distance between physical entanglements. We estimate the average distance between streptavidin proteins to be ~200 nm, and thus conclude that only a fraction of these proteins are actually engaged in crosslinking at any time. Yet, even in this limit of sparse connectivity, we find that crosslinking has a substantial effect on the ability of the deformation field to penetrate the sample. This suggests that long range stress transmission can be controlled by subtle changes in network architecture and connectivity. Moreover, the transition from non-affine to affine network deformation can be controlled by varying crosslinker concentration even under the application of very localized force fields.

Experimental

Proteins

Unlabeled and rhodamine-labeled tubulin proteins are generously provided by Professor Leslie Wilson at University of California, Santa Barbara. Unlabeled tubulin is purified from bovine brain by cycles of assembly and disassembly and followed by phosphocellulose chromatography.[40] Rhodamine-labeled tubulin is prepared by reaction with succinimidyl esters of carboxyrhodamine-6G (C-6157; Invitrogen). Commercial biotinylated porcine brain tubulin (T333P; Cytoskeleton, Inc.) with ~1 : 1 labeling ratio of biotin to tubulin heterodimer is reconstituted to 10 mg/mL in G-PEM80 buffer (80 mM PIPES, 4 mM $MgCl_2$, 1 mM EGTA and 1 mM GTP; pH = 6.9).

Preparation of MT networks embedded with magnetic beads

Entangled MT networks are formed by combining the following reagents on ice: unlabeled tubulin, rhodamine-labeled tubulin, 1 mM GTP, 1 mM DTT, 10% (v/v) DMSO, taxol and PEM80 (80 mM PIPES, 4 mM $MgCl_2$, 1 mM EGTA; pH = 6.9). Although the total tubulin concentration is varied in this study, in all cases, the molar ratios of rhodamine-labeled tubulin to total tubulin was 1 : 6, and taxol to total tubulin was 1 : 2. When making crosslinked MT networks, biotin-labeled tubulin is also included into the ice-cold tubulin mixture with the molar ratio of biotin-labeled to total tubulin of 1 : 7. In each case, tosyl-activated magnetic beads with diameter of 4.5 μm (Dynabeads, Invitrogen) are added to the ice-cold mixture at final concentration of ~10^6 beads/mL. To facilitate visualization of the deformation field induced by the motion of the magnetic bead, 2.5 μm latex beads (PS05N; Bangs Laboratories Inc) are sometimes embedded as probing beads at a final concentration of ~5 × 10^7 beads/mL.

The ice-cold tubulin solution is then loaded into small rectangular tubes (0.1 × 1 × 50 mm^3; Friedrich & Dimmock, Inc) by capillary action. Prior to loading, the capillary tubes are cleaned by rinsing with 1M sodium hydroxide, then pre-coated with reference beads to enable the subtraction of artefactual mechanical or thermal drift, or vibration of the sample and/or the stage from the real motion of the embedded magnetic particles. To achieve this, 5.43 μm latex beads (PS06N; Bangs Laboratories, Inc) are diluted in isopropanol to 5 × 10^5 beads/mL and loaded into the capillary tubes. The tubes are placed on a flat benchtop for 10 min to promote sedimentation. The tube is gently dried and the tube is baked at 150 °C for 2 min to partially melt the beads onto one side of the capillary tubes. After introduction to the capillary tube, entangled networks are immediately sealed with high vacuum grease, placed in a dry incubator at ~35 °C, and incubated for ~1 h under constant rotation to prevent the magnetic beads (and latex beads, if included) from settling. For crosslinked networks, the tubulin solution is first incubated at 35 °C for 3 min in a small microcentrifuge tube, then streptavidin is added such that the molar ratio of streptavidin: biotin-labeled tubulin is fixed at 1 : 10. The solution is well mixed by gently pipetting using a cut-off P20 pipette tip, then immediately loaded into the capillary tube, which is sealed with vacuum grease and incubated at 35 °C for ~1 h under constant rotation, as described above.

Confocal imaging for structure determination

Confocal microscopy images are obtained using an inverted Fluoview 500 laser scanning system (Olympus). Two-dimensional slices of rhodamine-labeled MT networks are imaged using 561 nm laser excitation and a 60× N.A. 1.4 oil-immersion

objective, with scan size of 1024 × 1024 pixels^2, scan rate of 9.59 s/scan, and magnification of 207.16 nm/pixel.

Image analysis

To quantify the mesh size of the MT networks, image analysis is performed on two-dimensional confocal images.[19,20] The images are first processed by thresholding. The threshold is chosen to remove as much noise as possible while retaining the pixels that correspond to the MTs. This is done by comparing intensities of the brightest background pixels to those of the dimmest MT pixels, with the background and MT pixels being differentiated by visual examination. After thresholding, the distance between nearest neighbour MT pixels within each row and column is determined. Our analysis is similar to the radial distribution of distances between filament intersections, but is implemented in Cartesian coordinates to take advantage of the natural axes of the microscope images. The distribution of distances is plotted and fitted to an exponential $P(\xi) = P_0 e^{-r/\xi}$, where r is the distance in microns and ξ is the characteristic mesh size (see Fig S6, ESI†). Each measurement is averaged over 28–57 images. Based on our pinhole and oil-immersion objective lens, we estimate our z-resolution to be ~1 μm. Using 2D images provides a good approximation of the average 3D mesh size, but underestimates the maximum pore diameter.[13]

Conventional magnetic tweezers

Mechanical measurements are performed using a custom-built magnetic tweezers system that enables precise manipulation of magnetic beads along the optical axis (the z-axis) and simultaneous three-dimensional tracking of bead position.[23] Briefly, a simple inverted microscope is constructed using an oil-immersion objective (100 ×, 1.25 N.A.) that is mounted onto a piezoelectric stage (*P*-725; Physik Instrumente) to enable nanopositioning of the focal plane. A 650 nm light emitting diode (Roithner Lasertechnik) provides illumination, and a CCD camera (CV-A10 CL; JAI) captures brightfield images at a frame rate of 60 Hz.

The applied magnetic field is generated by a pair of permanent rare-earth Neodymium Iron Boron (NdFeB) magnets (NS-505050; DuraMag) located above the sample stage, and oriented such that the alignment of their magnetic moments is antiparallel. Variation of the magnetic field (and thus magnetic force) at the sample plane is achieved by vertically translating the magnets with a DC-servo motor (M-126.PD1; Physik Instrumente). Separation distances between the sample plane and magnet may range from 0–24 mm from the sample plane. Forces are calibrated by measuring the Brownian motion of a magnetic bead that is tethered to the coverslip by a single DNA molecule, and thus acts as a simple inverted pendulum.[41] The lateral spring constant is given by the ratio of the vertical force to the DNA length. This spring constant can be found by modeling the measured bead trajectory with an overdamped Langevin equation of motion for a particle in a harmonic potential, and fitting the measured power spectrum in position to that predicted from the Langevin model after accounting for issues of finite data sampling rate and instrumental low-pass filtering.[42] The best-fit spring constant, along with the measured length, gives an estimate of the force; this calibration is then repeated at each desired magnet position. In this study, the minimum separation used was ~7 mm (corresponding to a force of ~33 pN on a typical 4.5-μm magnetic bead). Real-time tracking of the three-dimensional bead position is achieved using custom image analysis routines written in LABVIEW (National Instruments).[43] In the presence of the MT gels, we achieve a resolution of ~10 nm in the x and y directions and ~15–20 nm in the z direction.

Analysis of magnetic tweezers data

Analysis of data traces (as shown schematically in Fig. 2) is performed as follows. We dissect the bead motion into three distinct regimes—a short-time elastic jump, a relaxation transition, and a long-time creep regime. Creep velocity v is determined from the slope of a linear fit to bead displacement x *versus* time t for several (typically <10) seconds prior to the retraction of the magnet pair. We then determine the first order derivative of $x(t) - vt$. We define the elastic regime to start when the force is turned on and to end when the first order derivative reaches its maximum. This maximum also defines the beginning of the relaxation regime, which ends when the derivative drops to zero. For practical purposes, we define the end point by the time at which the moving average of the derivative drops below a threshold equal to 0.05% of the maximum value. The moving average is implemented using a Savitzky–Golay smoothing filter (polynomial order 2, 20 point window). The flow regime follows and ends when the force is reduced at time $t = T$. After identifying these regimes, the following parameters are calculated: d_1 is the distance the bead travels in the elastic regime and τ is the total time of the relaxation regime. When the magnets are retracted, we identify an elastic recovery regime that starts when the force is turned off and ends when the first order derivative reaches its minimum; d_2 is the distance the bead travels in this second elastic regime. All uncertainties are reported as SEM values.

Portable magnetic tweezers to determine structure–mechanics relationships

A newly-designed, custom-built portable magnetic tweezers device is used to apply calibrated stresses to microtubule networks, while their microscale deformation is simultaneously measured using confocal microscopy.[24] Briefly, two NdFeB rare earth magnets (N45, 0.25 × 0.25 × 1 inch^3; Applied Magnets) are mounted onto a two-axis translation stage and positioned near the focus of the objective lens in a manner that protects the imaging quality of the microscope. The distance between the magnets and sample is controllably varied, leading to application of controlled forces to small magnetic particles at the sample plane. For a typical measurement, the magnets are moved toward the sample until they just touch the coverslip edge, to ensure application of the maximum force (which we call the 'force-on' condition). To reduce this force level, the magnets are moved away from the coverslip surface until the separation distance exceeds ~10 mm (which we call the 'force-off' condition). The rate of magnet retreat (and therefore of the rate of force reduction) can be varied through manual control of the translation stage. Forces are calibrated by measuring the velocity at which a free bead moved through a liquid of known viscosity

using Stokes Law. At each force condition, the deformation of the microtubule networks and detailed interaction between the magnetic bead and the surrounding microtubule mesh are recorded using confocal microscopy. In this 'sideways-pulling' geometry, beads move perpendicular to the optical axis (the 'x' axis) when the force is on. Images are obtained using both the fluorescence (561 nm laser excitation) and the transmitted light channels using either a 60×, 1.4 N.A. oil-immersion objective lens or a 60×, 1.2 N.A. water-immersion objective lens with coverslip thickness correction collar. A time series of two-dimensional image stacks is collected using a scan size of 512 × 512 pixels^2 at a rate of 1.12 s/scan (4× digital zoom, magnification 103.6 nm/pixel).

Conclusions

We use a new experimental approach to measure structure-mechanics relationships in reconstituted MT cytoskeletons. We apply localized forces directly to MT gels in a physiologically-relevant manner using magnetic tweezers devices while observing network deformation using confocal microscopy. At short times, entangled gels are elastic, with gentle stiffening observed above ~70% strains, which we attribute to a densification of the network in front of the bead. For entangled gels, network deformation is nonaffine, resulting primarily in bending of MTs near the particle surface. Crosslinking leads to a much more uniform deformation field that penetrates over distances of several particle diameters. This indicates that the spatial extent of the deformation field depends sensitively on network architecture and connectivity, and that even sparse crosslinking of networks can have a significant effect on long-range stress transmission.

Acknowledgements

Authors thank A. Levine and R. Shlomovitz for many helpful discussions, and are grateful for the support of a Burroughs Wellcome Fund Career Award at the Scientific Interface (to MTV), a Special Research Award from Santa Barbara Cottage Hospital (to MTV), a Young Investigators Grant from the Human Science Frontiers Program (RGY0078/2007-C to OAS), and a National Institutes of Health/National Center for Research Resources (NIH/NCRR) Shared Instrumentation Grant (1S10RR017753-01).

References

1 N. Hirokawa, Y. Noda, Y. Tanaka and S. Niwa, *Nat. Rev. Mol. Cell Biol.*, 2009, **10**, 682–696.
2 K. Kalil and E. W. Dent, *Curr. Opin. Neurobiol.*, 2005, **15**, 521–526.
3 E. W. Dent and K. Kalil, *Journal of Neuroscience*, 2001, **21**, 9759–9769.
4 O. C. Rodriguez, A. W. Schaefer, C. A. Mandato, P. Forscher, W. M. Bement and C. M. Waterman-Storer, *Nat. Cell Biol.*, 2003, **5**, 599–609.
5 C. Waterman-Storer, D. Y. Duey, K. L. Weber, J. Keech, R. E. Cheney, E. D. Salmon and W. M. Bement, *J. Cell Biol.*, 2000, **150**, 361–376.
6 S. Kim and P. A. Coulombe, *Nat. Rev. Mol. Cell Biol.*, 2010, **11**, 75–81.
7 I. Kaverina, O. Krylyshkina, K. Beningo, K. Anderson, Y.-L. Wang and J. V. Small, *Journal of Cell Science*, 2002, **115**, 2283–2291.
8 A.-M. C. Yvon, D. J. Gross and P. Wadsworth, *Proc. Natl. Acad. Sci. U. S. A.*, 2001, **98**, 8656–8661.
9 A. Musacchio and E. D. Salmon, *Nat. Rev. Mol. Cell Biol.*, 2007, **8**, 379–393.
10 C. P. Brangwynne, F. C. MacKintosh and D. A. Weitz, *Proc. Natl. Acad. Sci. U. S. A.*, 2007, **104**, 16128–16133.
11 F. Gittes, B. Mickey, J. Nettleton and J. Howard, *J. Cell Biol.*, 1993, **120**, 923–934.
12 P. A. Janmey, U. Euteneuer, P. Traub and M. Schliwa, *J. Cell Biol.*, 1991, **113**, 155–160.
13 Y.-C. Lin, G. H. Koenderink, F. C. MacKintosh and D. A. Weitz, *Macromolecules*, 2007, **40**, 7714–7720.
14 V. Pelletier, N. Gal, P. Fournier and M. L. Kilfoil, *Phys. Rev. Lett.*, 2009, **102**, 188303.
15 M. Sato, W. H. Schwartz, S. C. Selden and T. D. Pollard, *J. Cell Biol.*, 1988, **106**, 1205–1211.
16 A. C. Maggs, *Phys. Rev. E: Stat. Phys., Plasmas, Fluids, Relat. Interdiscip. Top.*, 1998, **57**, 2091.
17 D. A. Head, A. J. Levine and F. C. MacKintosh, *Phys. Rev. E: Stat., Nonlinear, Soft Matter Phys.*, 2005, **72**, 061914.
18 M. Bai, A. R. Missel, A. J. Levine and W. S. Klug, *Acta Biomater.*, 2011, **7**, 2109–2118.
19 L. J. Kaufman, C. P. Brangwynne, K. E. Kasza, E. Filippidi, V. D. Gordon, T. S. Deisboeck and D. A. Weitz, *Biophys. J.*, 2005, **89**, 635–650.
20 Y.-l. Yang and L. J. Kaufman, *Biophys. J.*, 2009, **96**, 1566–1585.
21 P. G. deGennes, P. Pincus, R. M. Velasco and F. Brochard, *J. Phys.*, 1976, **37**, 1461–1473.
22 M. Manosas, A. Meglio, M. M. Spiering, F. Ding, S. J. Benkovic, F. X. Barre, O. A. Saleh, J. F. Allemand, D. Bensimon and V. Croquette, *Methods Enzymol.*, 2010, **475**, 297–320.
23 N. Ribeck and O. A. Saleh, *Rev. Sci. Instrum.*, 2008, **79**, 6.
24 Y. Yang, J. Lin, R. Meschewski, E. Watson and M. T. Valentine, *BioTechniques*, 2011, **51**, 29–34.
25 M. Doi and S. F. Edwards, *The theory of polymer dynamics*, Oxford University Press, Oxford, 1986.
26 C. Storm, J. J. Pastore, F. C. MacKintosh, T. C. Lubensky and P. A. Janmey, *Nature*, 2005, **435**, 191–194.
27 J. Uhde, W. Feneberg, N. Ter-Oganessian, E. Sackmann and A. Boulbitch, *Phys. Rev. Lett.*, 2005, **94**, 198102.
28 M. L. Gardel, J. H. Shin, F. C. MacKintosh, L. Mahadevan, P. Matsudaira and D. A. Weitz, *Science*, 2004, **304**, 1301–1305.
29 K. M. Schmoller, O. Lieleg and A. R. Bausch, *Biophys. J.*, 2009, **97**, 83–89.
30 K. M. Schmoller, O. Lieleg and A. R. Bausch, *Soft Matter*, 2008, **4**, 2365–2367.
31 O. Lieleg, J. Kayser, G. Brambilla, L. Cipelletti and A. R. Bausch, *Nat. Mater.*, 2011, **10**, 236–242.
32 K. M. Schmoller, P. Fernandez, R. C. Arevalo, D. L. Blair and A. R. Bausch, *Nat. Commun.*, 2010, **1**, 134.
33 T. M. Squires and T. G. Mason, *Annu. Rev. Fluid Mech.*, 2010, **42**, 413–438.
34 N. Y. Yao, C. P. Broedersz, Y. Lin, K. E. Kasza, F. C. MacKintosh and D. A. Weitz, *Biophys. J.*, 2010, **98**, 2147–2153.
35 G. Z. Sowa, D. S. Cannell, A. J. Liu and E. Reisler, *J. Phys. Chem. B*, 2006, **110**, 22279–22284.
36 J. Tang and P. Janmey, *Biol. Bull.*, 1998, **194**, 406–408.
37 C. Semmrich, T. Storz, J. Glaser, R. Merkel, A. R. Bausch and K. Kroy, *Proc. Natl. Acad. Sci. U. S. A.*, 2007, **104**, 20199–20203.
38 Y.-C. Lin, G. H. Koenderink, F. C. MacKintosh and D. A. Weitz, *Soft Matter*, 2011, **7**, 902–906.
39 L. A. Hough, M. F. Islam, P. A. Janmey and A. G. Yodh, *Phys. Rev. Lett.*, 2004, **93**, 168102.
40 L. Wilson and J. J. Correia, in *Methods in Cell Biology, Vol. 95*, Elsevier Academic Press Inc, 2010, pp. 2–15.
41 T. R. Strick, J. F. Allemand, D. Bensimon, A. Bensimon and V. Croquette, *Science*, 1996, **271**, 1835–1837.
42 K. Neuman and A. Nagy, *Nat. Methods*, 2008, **5**, 491–505.
43 C. Gosse and V. Croquette, *Biophys. J.*, 2002, **82**, 3314–3329.

